Microgrid Service Restoration Incorporating Unmonitored Automatic Voltage Controllers and Net Metered Loads

Akshay Kumar Jain[1], *Graduate Student Member, IEEE*, Chen-Ching Liu[1], *Life Fellow, IEEE*, Kevin P. Schneider[2], *Fellow, IEEE*, Francis K. Tuffner[2], *Senior Member, IEEE*, Dan Ton[3]

***Abstract* - Islanded microgrids may experience voltage and frequency instability due to uncontrolled state changes of voltage regulation devices and inaccurate demand forecasts. Uncontrolled state changes can occur if optimal microgrid restoration and dispatch algorithms, used for generating control commands for distributed energy resources, do not incorporate the behavior of automatic controllers of voltage regulation devices. Inaccurate demand forecasts may be encountered since post-outage demand of behind-the-meter net metered (NM) loads can vary significantly from their historical NM profiles. This paper proposes an optimization formulation which allows optimal control of voltage regulators and capacitor banks without remote control and communication capabilities. A generalized demand model for NM loads is proposed which incorporates the cold load pickup phenomenon and their time varying post-outage demand in accordance with the IEEE 1547 standard. The time dependent optimal control formulation and the NM demand model are integrated in a sequential microgrid restoration algorithm by linearization of the involved logic propositions. A detailed case study on the unbalanced IEEE 123-node test system in OpenDSS validates the effectiveness of the proposed approach.**

***Index Terms* - Demand Forecasting, Microgrids, Optimization, Power System Restoration.**

NOMENCLATURE

$\mathcal{G}(\mathcal{B},\mathcal{E})$	Directed graph of the 3-phase microgrid; set of all nodes $\mathcal{B}$ and edges $\mathcal{E}$.
θ	represents the phases $\theta \in \{a,b,c\}$.
$P_{ij}^{\theta}(Q_{ij}^{\theta})$	Per phase real (reactive) power flow of edge $ij \in \mathcal{E}$.
V_i^{θ}	Per phase nodal voltage of node $i \in \mathcal{B}$.
$P_{ij}^{L,\theta}(Q_{ij}^{L,\theta})$	Per phase real (reactive) demand at node $i \in \mathcal{B}$ at time step k.
$P_{ij}^{G,\theta}(Q_{ij}^{G,\theta})$	Per phase real (reactive) generation at node $i \in \mathcal{B}$ at time step k.
$\mathcal{C},\mathcal{C}_{\mathrm{c}}$	Set of 3-phase capacitor bank nodes, set of controllable capacitor bank nodes.
$\bar{Q}_i^{C,\theta}$	Per phase kVA rating of capacitor bank $i \in \mathcal{C}$. Bar over symbols represents a parameter.
$Q_{c,i}^{\theta}$	Per phase capacitive injection at node $i \in \mathcal{B}$.
$\mathcal{E}_{\mathrm{R}}$	Set of 3-phase edges with AVRs.
$\mathcal{K}$	Set of restoration time steps $\mathcal{K} := \{1,..,K\}$.
$\bar{r}_{ij}^{\theta}(\bar{x}_{ij}^{\theta})$	Per phase resistance (reactance) of edge $ij \in \mathcal{E}$.
δ_{ij}^{E}	Energization status of edge $ij \in \mathcal{E}$.
δ_{ij}^{N}	Energization status of node $i \in \mathcal{B}$.

INTRODUCTION

Microgrids are essential building blocks for creating resilient distribution systems against extreme events such as weather events and cyberattacks [1]. Optimal dispatch and energy supply restoration after an outage using locally available distributed energy resources (DERs) are critical microgrid functions [2]. However, current microgrid restoration and dispatch algorithms do not accurately incorporate the impact of key microgrid components such as automatic voltage regulators (AVRs) and capacitor banks [3],[4]. Non dispatchable behind-the-meter (BTM) resources such as net metered (NM) loads which have a load and a photovoltaic (PV) system are also not adequately considered [5]. Uncontrolled operation of voltage regulation devices combined with a demand generation imbalance due to inaccurate demand forecasts of NM loads can lead to frequency instability in islanded microgrids [6].

Microgrids are typically integrated with radial distribution feeders [7] and can have AVRs and capacitor banks. However, the discrete behavior of these devices introduces non-linearities and is often not considered in microgrid service restoration and dispatch algorithms [4]. Lack of coordination between automatically controlled voltage regulation devices and centrally dispatched DERs can lead to voltage instability in islanded microgrids due to significant increases in state changes of AVRs [8],[9] and capacitor banks [10]. Even when these devices are included in microgrid restoration and dispatch algorithms, their taps are either assumed to be stationary during restoration [11] or are considered as decision variables [12]. This assumes remote control capabilities are present in these devices. This, however, is not true and most AVRs and capacitor banks deployed in rural and semi-urban feeders rely on automatic controllers [13],[14]. Upgrading their controllers with intelligent electronic devices can be costly [15]. The high cost can cause microgrid deployments to become infeasible, especially in rural and disadvantaged communities. It is thus essential to accurately incorporate the behavior of these automatic voltage controllers within microgrid dispatch and restoration optimization algorithms.

This work was supported by the U.S. Department of Energy (DOE) Office of Electricity through the Pacific Northwest National Laboratory (PNNL).

[1]A.K. Jain and C.C. Liu are with the Bradley Department of Electrical and Computer Engineering, Virginia Tech, Blacksburg, VA, 24060, USA, e-mail: (akjain, ccliu)@vt.edu.

[2]Kevin P. Schneider and Francis K. Tuffner are with the Pacific Northwest National Laboratory (PNNL), Washington, USA. Email: (kevin.schneider, Francis.Tuffner)@pnnl.gov

[3]Dan Ton is with U.S. Department of Energy (DOE) Office of Electricity (OE). Email: Dan.Ton@hq.doe.gov

The presence of more than a million NM loads in California alone [16] suggests that high penetration of NM loads can be expected in distribution systems and microgrids. The BTM PV system of these NM loads is not dispatchable as this would require an extensive communication network and control capabilities [17]. For NM loads only the net demand (actual demand - generation) may be available through advanced metering infrastructure (AMI) [18]. However, even with AMI, the demand of NM loads during microgrid service restoration cannot be forecasted in accordance with the IEEE 1547-2018 standard [19].

NM loads typically exhibit the Cold Load Pickup (CLPU) phenomenon during restoration. CLPU refers to the increase in load demand observed after an outage due to the loss of diversity of thermostatically controlled loads (TCLs) [20]. Since NM loads consist of a PV system and a typical residential or commercial load, most NM loads can be expected to have TCL loads which will exhibit CLPU phenomenon after an outage. The behavior of TCL loads is typically characterized using the delayed exponential model (DEM) [21]. More recently it has been shown that the DEM model is not accurate for shorter outage durations [22]. However, a generalized model incorporating both CLPU and NM load behavior during restoration has not been reported before.

In this paper, it will be shown in section III, that modeling both CLPU and NM load behavior during restoration requires the disaggregation of NM time series of NM loads into actual demand and generation time series. Disaggregation has been studied recently for demand response applications but not for microgrid restoration [23]. It has been used to estimate the rating of PV systems, which however is known to utilities through interconnection applications [24]. In [25] solar generation and actual demand for each NM load are forecasted separately, by representing them as linear functions of representative feature vectors. The feature vector for solar generation is the average profile of several randomly located NM loads deployed with separate solar generation measurement meters. The actual demand feature vector is the average of the demand profiles of the loads without solar generation. However, no justifications are provided for using linear functions. Accuracy is not ensured, as randomly placed solar generation measurement meters are used. Also, since load demands can vary widely amongst NM loads, separate load forecasts introduce forecasting errors. The contributions of this paper which address these issues are:

- A novel optimal DER dispatch method is proposed which creates such voltages and line flows at the point of common coupling (PCC) of voltage regulation devices, commanding their unmonitored automatic voltage controllers tomove to their respective optimal states.
- A generalized time dependent demand model is proposed for NM loads which incorporates both CLPU and their behavior during microgrid restoration. The model uses the correlation in NM time series of NM loads to obtain the disaggregated actual demand and generation time series.
- A mixed integer linear programming (MILP) based approach is proposed to accurately control the time dependent behavior of voltage regulation devices and NM loads during each restoration time interval by linearizing the logic propositions.

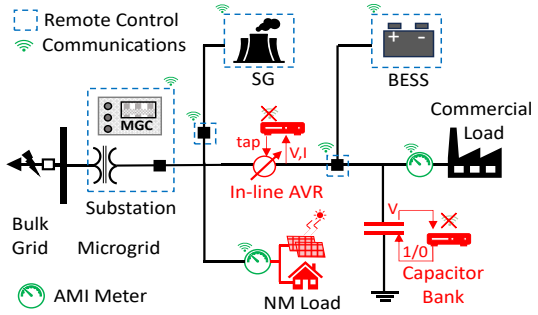

Fig. 1. Typical microgrid topology with unmonitored automatic voltage controllers, NM loads and remotely controllable DERs and switches.

The proposed approach can be integrated with existing MILP based microgrid restoration algorithms [26].

The remaining of this paper is organized as follows: Section II describes the proposed optimal DER dispatch method for controlling unmonitored automatic voltage regulation devices. Section III presents the proposed generalized NM load demand model. The proposed MILP based sequential microgrid restoration approach incorporating automatic voltage regulation devices and NM loads is presented in section IV. A case study on an unbalanced model of the IEEE 123-node test feeder in OpenDSS [27] presented in section V demonstrates the effectiveness of the proposed approach.

Optimal Control Incorporating Unmonitored Automatic Voltage Controllers

Voltage regulation devices such as AVRs and capacitor banks may have automatic controllers. Based on the measured value of a local control parameter (typically voltage), the controller determines the control action. The control action for AVRs is a change in the tap position. The control action for capacitor banks is turning them ON or OFF based on the value of the control parameter. These devices are automatic and hence their states are not available to the centralized controller via AMI, nor can these be controlled remotely, as illustrated in Fig. 1.

The main contribution here is the development of an integrated approach for optimal control of these devices. Linearized constraints are developed which relate the AVR's local controller's operation principle with the determined optimal tap positions and DER dispatches. Constraint selection is then automated based on the sign of the optimal tap position. Optimal control of capacitor banks is achieved using a similar approach. Additional constraints required for integrating the proposed optimal control approach with MILP based sequential microgrid restoration algorithms are presented in section IV. All these constraints are integrated and solved simultaneously.

A. Determining Optimal States

The optimal states of AVRs and capacitor banks can be obtained in the same manner irrespective of whether these devices have remote control capabilities. For an AVR connected between nodes k and j, $k \to j$, the voltages on these nodes may be expressed as $V_j^\theta = a_{kj}^\theta V_k^\theta$, where a_{kj}^θ is the tap position of the AVR on phase $\theta \in \{a,b,c\}$. Here the loss term $(\bar{r}_{kj}^\theta P_{kj}^\theta + \bar{x}_{kj}^\theta Q_{kj}^\theta)$ present in the linearized *DistFlow* power flow model [28] are ignored. a_{kj}^θ can only take discrete integer values in the

range ± 16. These taps provide ± 0.1 p.u. voltage regulation with a 0.00625 p.u. step. These 33 tap positions can be expressed using a 6-bit code [29], which significantly reduces the number of binary variables needed from 33 to 6 for every single phase AVR. For instance, the code 100000 represents tap +16, code 000000 represents tap -16 and code 010000 represents tap 0 or the neutral position. Thus, the linearized voltage constraint for an AVR connected between nodes k and j is given by (1).

$$V_j^\theta = V_k^\theta \left(0.9 + 0.00625 \sum_{n=0}^{5} \delta_{kj,n}^\theta (2)^n\right), \delta_{kj,n}^\theta \in \{0,1\}, kj \in \mathcal{E}_R \quad (1)$$

The products of binary variables $\delta_{kj,n}^\theta, n \in \{0,..,5\}$ and the continuous voltage variable V_k^θ are linearized (2) using McCormick linearization [30]. The required upper and lower limits of the continuous variable are set as the voltage limits $(\bar{V}^l, \bar{V}^u)$. The same linearization approach is used henceforth to linearize products of binary and continuous variables.

$$\bar{V}^l \delta_{kj,n}^\theta \le x_{kj,n}^\theta \le \bar{V}^u \delta_{kj,n}^\theta, \text{ where } x_{kj,n}^\theta = \delta_{kj,n}^\theta V_k^\theta$$
$$V_k^\theta - \left(1 - \delta_{kj,n}^\theta\right)\bar{V}^u \le x_{kj,n}^\theta \le V_k^\theta - \left(1 - \delta_{kj,n}^\theta\right)\bar{V}^l \quad (2)$$

Maximum allowable tap positions are restricted to 33 using (3). For gang operated AVRs, taps on all three phases are constrained to be equal by adding $\delta_{kj,n}^a = \delta_{kj,n}^b = \delta_{kj,n}^c$.

$$\sum_{n=0}^{5} \delta_{kj,n}^\theta (2)^n \le 32, \; kj \in \mathcal{E}_R \quad (3)$$

The state of a controllable capacitor bank $\delta_{c,i}^\theta, i \in \mathcal{C}_c$ is included in the reactive power flow expression of the *DistFlow* model as shown in (4).

$$\sum_{h:h\to i} Q_{hi}^\theta = \sum_{j:i\to j} Q_{ij}^\theta + Q_i^{L,\theta} + Q_i^{G,\theta} + \delta_{c,i}^\theta \bar{Q}_i^{C,\theta}, \; \forall i \in \mathcal{C}_c \quad (4)$$

Upon solving the MILP dispatch or restoration algorithm after including constraints (1)-(4), the optimal AVR tap positions $\hat{a}_{kj}^\theta = 0.9 + 0.00625 \sum_{n=0}^{5} \delta_{kj,n}^\theta (2)^n, \; kj \in \mathcal{E}_R$ and optimal capacitor banks states $\hat{\delta}_{c,i}^\theta, i \in \mathcal{C}_c$ are obtained. If AVRs and capacitor banks have remote control capabilities, then these optimal states can be directly communicated to them. This, however, is not true for most rural and semi-urban distribution feeders and microgrids. The optimal control approach proposed in this paper generates optimal DER dispatches which indirectly influence the automatic controllers of the AVRs and capacitor banks to move to these optimal states.

B. Linearizing AVR Load Center Voltage Estimation

AVRs use a line drop compensator (LDC) circuit to estimate the voltage at their load center [13]. The primary (c_{kj}^p) and secondary (c_{kj}^s) turns ratio of the current transformer, turns ratio of the potential transformer (p_{kj}) and the compensator impedance settings in volts $(r_{kj}^{\theta,v}, x_{kj}^{\theta,v})$ of the LDC of any AVR connected between nodes k and $j, kj \in \mathcal{E}_R$ are known. Using these pre-determined settings, the LDC estimates the voltage at its load center $(V_{kj}^{r,\theta})$ using (5).

$$V_{kj}^{r,\theta} = \frac{V_j^\theta}{p_{kj}} - \frac{I_{jh}^\theta c_{kj}^s}{c_{kj}^p} \times \left(r_{kj}^{\theta,v} + i x_{kj}^{\theta,v}\right) \quad (5)$$

To be able to indirectly influence the LDC, it is important to add (5) as a constraint. Upon conversion to per unit quantities, the LDC estimates the voltage drop to the load center as $I_{jh}^\theta \times \left(r_{kj}^{\theta,v} + i x_{kj}^{\theta,v}\right)$. However, current is not a variable in linearized power flow models such as the *DistFlow* model. Including current by using $I_{jh}^\theta = \frac{\left(P_{jh}^\theta + iQ_{jh}^\theta\right)^*}{\left(V_j^\theta\right)^*}$ and using the complex impedance will introduce non-linearities. A closer examination of the voltage drop expression of the *DistFlow* model $V_j^\theta = V_h^\theta + \bar{r}_{jh}^\theta P_{jh}^\theta + \bar{x}_{jh}^\theta Q_{jh}^\theta$, between any two nodes j and h shows that it approximates the voltage drop across the line as $\Delta V_{jh}^\theta = I_{jh}^\theta \times \left(r_{jh}^\theta + i x_{jh}^\theta\right) \approx P_{jh}^\theta r_{jh}^\theta + Q_{jh}^\theta x_{jh}^\theta$. The same can be used to approximate the voltage drop till the AVR's load center after converting to per unit quantities as $I_{jh}^\theta \times \left(r_{kj}^{\theta,v} + i x_{kj}^{\theta,v}\right) \approx P_{jh}^\theta r_{kj}^{\theta,l} + Q_{jh}^\theta x_{kj}^{\theta,l}$. Here $r_{kj}^{\theta,l} + i x_{kj}^{\theta,l} = \left(r_{kj}^{\theta,v} + i x_{kj}^{\theta,v}\right) \times p_{kj}/c_{kj}^p$ represents the LDC's estimated line impedance till the load center. Thus, the voltage at the load center can be estimated to be $V_{kj}^{r,\theta} = V_j^\theta - P_{jh}^\theta r_{kj}^{\theta,l} - Q_{jh}^\theta x_{kj}^{\theta,l} = \mathcal{T}_1$.

C. Constraints to Influence AVRs to Move to Optimal Tap Positions

LDC sends commands to change taps if $V_{kj}^{r,\theta}$ falls outside $V_{kj}^{\theta,l} \pm D_{kj}^{\theta,l}/2$, where $V_{kj}^{\theta,l}$ is the desired load center voltage setting and $D_{kj}^{\theta,l}$ is the allowable deadband. If $V_{kj}^{r,\theta} < \left(V_{kj}^{\theta,l} - D_{kj}^{\theta,l}/2\right)$, then taps are increased by rounding $a_{kj}^\theta = \left(V_{kj}^{\theta,l} - D_{kj}^{\theta,l}/2 - V_{kj}^{r,\theta}\right)/0.00625$ to the nearest integer. Thus, if $\hat{a}_{kj}^\theta$ is evaluated to be higher than the neutral tap position by the MILP dispatch or restoration algorithm, then the voltage at the load center should be $V_{kj}^{r,\theta} = V_{kj}^{\theta,l} - D_{kj}^{\theta,l}/2 - \hat{a}_{kj}^\theta \times 0.00625$, in order to make the LDC to command the AVR to move to $\hat{a}_{kj}^\theta$. Here $V_{kj}^{r,\theta}$ is replaced with $\mathcal{T}_1 = \left(V_j^\theta - P_{jh}^\theta r_{kj}^{\theta,l} - Q_{jh}^\theta x_{kj}^{\theta,l}\right)$ and $\hat{a}_{kj}^\theta \times 0.00625$ is replaced with $\mathcal{T}_2 = \left(\left(0.9 + 0.00625 \sum_{n=0}^{5} \delta_{kj,n}^\theta (2)^n\right) - 1\right)$. Thus, the equality constraint to be added to move an AVR to higher tap positions is given by (6). That is, (6) constrains DER dispatches to create the PCC voltages and line flows for each AVR to make them move to $\hat{a}_{kj}^\theta$.

$$\mathcal{T}_1 = V_{kj}^{\theta,l} - D_{kj}^{\theta,l}/2 - \mathcal{T}_2 \quad (6)$$

Similarly, if $V_{kj}^{r,\theta} > \left(V_{kj}^{\theta,l} + D_{kj}^{\theta,l}/2\right)$, then LDC commands the AVR taps to be decreased by rounding $\left(V_{kj}^{r,\theta} - V_{kj}^{\theta,l} - D_{kj}^{\theta,l}/2\right)/0.00625$ to the nearest integer. Thus, if $\hat{a}_{kj}^\theta$ is evaluated to be lower than the neutral tap tap position, then the voltage at the load center should be $V_{kj}^{r,\theta} = V_{kj}^{\theta,l} + D_{kj}^{\theta,l}/2 + \hat{a}_{kj}^\theta \times 0.00625$. Thus, the equality constraint to be added to move an AVR to lower tap positions is given by (7).

$$\mathcal{T}_1 = V_{kj}^{\theta,l} + D_{kj}^{\theta,l}/2 - \mathcal{T}_2 \quad (7)$$

D. Automating Constraint Selection

Based on whether AVR taps have to be increased (6) or decreased (7), a different constraint needs to be applied. Since

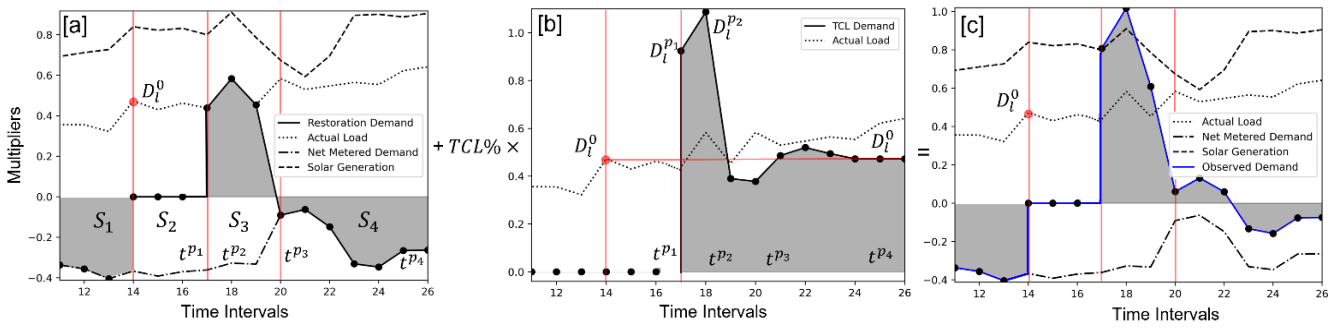

Fig. 2. [a] NM demand stages during restoration; [b] demand increase due to CLPU; [c] proposed NM load demand model (CLPU + NM demand stages)

tap positions $\hat{a}_{kj}^{\theta}$ are decision variables, an approach is needed to automatically select the correct constraint. It is achieved here by making use of the 6-bit binary code used for determining the optimal tap positions in (1). As mentioned, the code 010000 represents the neutral tap position. Thus, the fifth binary variable $\delta_{kj,4}^{\theta}, kj \in \mathcal{E}_R$ must be 1 for all positive tap positions. The only exception is the $+16^{\text{th}}$ tap position for which $\delta_{kj,4}^{\theta} = 0$ but $\delta_{kj,5}^{\theta} = 1$. It should be noted that it is only because of the 6-bit code that a single binary variable $(\delta_{kj,4}^{\theta}, kj \in \mathcal{E}_R)$ allows automatic selection of the correct constraint. If 33 binary variables were used to represent each tap, all 33 binary variables would have to be considered, further increasing the computational complexity. Thus, to select the correct constraint automatically, (6) and (7) are replaced with (8)-(10), where M is a large number.

$$-M\left(1-\delta_{kj,4}^{\theta}\right) \le \mathcal{T}_1 - V_{kj}^{\theta,l} + D_{kj}^{\theta,l}/2 + \mathcal{T}_2 \le M\left(1-\delta_{kj,4}^{\theta}\right) \quad (8)$$

$$-M\left(1-\delta_{kj,5}^{\theta}\right) \le \mathcal{T}_1 - V_{kj}^{\theta,l} + D_{kj}^{\theta,l}/2 + \mathcal{T}_2 \le M\left(1-\delta_{kj,5}^{\theta}\right) \quad (9)$$

$$-M\sum_{n=4}^{5}\delta_{kj,n}^{\theta} \le \mathcal{T}_1 - V_{kj}^{\theta,l} - D_{kj}^{\theta,l}/2 + \mathcal{T}_2 \le M\sum_{n=4}^{5}\delta_{kj,n}^{\theta} \quad (10)$$

E. Optimal Control of Automatic Capacitor Banks

Capacitor banks switch ON when their PCC voltage falls below a threshold $(V_i^{\theta} < V_i^{\theta,on}, i \in \mathcal{C}_c)$ and turn OFF when their PCC voltage exceeds a threshold $(V_i^{\theta} > V_i^{\theta,of}, i \in \mathcal{C}_c)$. Based on the optimally evaluated state of the capacitor bank $\hat{\delta}_{c,i}^{\theta}, i \in \mathcal{C}_c$, constraints (11) and (12) ensure turn ON or OFF the capacitor bank.

$$-M\left(1-\delta_{c,i}^{\theta}\right) \le V_i^{\theta} - V_i^{\theta,on} \le M\left(1-\delta_{c,i}^{\theta}\right) \quad (11)$$

$$-M\delta_{c,i}^{\theta} \le V_i^{\theta} - V_i^{\theta,of} \le M\delta_{c,i}^{\theta} \quad (12)$$

NET METERED LOAD MODEL

Demand generation imbalance due to inaccurate demand forecasts can impact the stability of a microgrid during service restoration. It is shown here that net-metered (NM) load demand can vary significantly during restoration from their historical profiles. For any NM load the net demand $(p_{i,t}^{n})$ at any time t is available via AMI and is related to the actual demand $(p_{i,t}^{d})$ and solar generation $(p_{i,t}^{g})$ by (13).

$$p_{i,t}^{n} = p_{i,t}^{d} - p_{i,t}^{g} \quad (13)$$

It will be shown here that the disaggregation of this NM time series into actual demand and generation time series is essential for including Cold Load Pickup (CLPU) phenomenon and demand stages during microgrid restoration. The main contribution is the development of a generalized time dependent NM load demand model, which completely describes the behavior of NM loads during microgrid restoration in accordance with the IEEE 1547 standard and incorporates the CLPU phenomenon.

A. Cold Load Pickup Phenomenon (CLPU) and NM loads

In the CLPU model here [22], as shown in Fig. 2 [b], the TCL demand is $D_l^{p_1}$ when it is restored at time point t^{p_1}. The demand then increases linearly to peak demand $D_l^{p_2}$ at t^{p_2}, as more TCLs turn ON. $D_l^{p_1} < D_l^{p_2}$ as diversity is not completely lost due to the short outage duration. The demand then decreases gradually to the pre-outage demand level D_l^0 and stays there after t^{p_4} as TCL diversity is restored. The behavior between time points t^{p_2} and t^{p_4} can be modeled using a polynomial function $h(y)$. Using the DEM model as the basis, the complete CLPU curve is modeled using (14)-(16), for any time $k \in \mathcal{K}$ with a Δt time step between restoration intervals [22].

$$G_l(k) = \left[D_l^{p_1} + \frac{D_l^{p_2} - D_l^{p_1}}{t^{p_2} - t^{p_1}}(k-1)\Delta t\right]\left(1 - x\left(R_{l,k}^1\right)\right) + h\left(R_{l,k}^1\right)x\left(R_{l,k}^1\right)\left(1 - x\left(R_{l,k}^2\right)\right) + x\left(R_{l,k}^2\right)D_l^0 \quad (14)$$

where $x(j), R_{l,k}^1$ and $R_{l,k}^2$ are defined as,

$$x(j) = \begin{cases} 1 & \text{,if } j > 0 \\ 0 & \text{,if } j \le 0 \end{cases} \quad (15)$$

$$R_{l,k}^1 = (k-1)\Delta t - (t^{p_2} - t^{p_1}),\ R_{l,k}^2 = (k-1)\Delta t - (t^{p_4} - t^{p_1}) \quad (16)$$

Equation (17) shows that this CLPU model is a function of the pre-outage demand D_l^0. The challenge however with NM loads is that only the net demand is available, whereas D_l^0 is a function of the actual demand. This requires disaggregation of net-metered demand time series into actual demand and solar generation time series.

B. Microgrid Restoration Stages with NM Loads

The demand observed for an NM load during the restoration process, as shown in Fig. 2[a], can be divided into four stages. Prior to the outage, in stage S_1, the net demand is available. In stage S_2, the load is de-energized. S_2 continues until the NM load is energized by the restoration algorithm. In stage S_3, when the NM load is restored, the actual demand is observed instead of net demand. This is because the PV systems stay offline due to their default *'enter service delay'* as per IEEE 1547-2018 [19]. Finally, in stage S_4, PV systems come back online after their '*enter service delay*' and the net metered demand is

observed. Stage S_3 is critical, as sudden energization of loads create transients. Inaccurate dispatch of DERs based on net demand forecasts can lead to frequency instability [6] and restoration failure. This further necessitates disaggregation of NM time series.

C. Disaggregation of Net Metered Time Series

Loads in a microgrid cannot be restored individually as all loads are not connected via remotely operable switches. As shown in Fig. 3, all the NM loads downstream of a switch, referred to as a load section (LS), are energized together [21],[31]. Given NM time series of all the loads in a LS, and the forecast for either their solar generation or actual demand, the other can be obtained by taking the difference. The problem then is to estimate both solar generation and actual demand of each NM load in a LS given only their NM time series.

In this paper, a systematic approach is proposed for placing a solar generation measurement meter based on correlation in historical NM time series data, for disaggregating the solar generation and actual demand of each NM load. The correlation coefficient $\eta_{i,j}$ between any i^{th} and j^{th} NM loads can be found by taking the ratio of the covariance $c_{i,j}$ with the standard deviations s_i and s_j of their historical net metered time series of length N. $\tilde{p}_i^n, \tilde{p}_j^n$ are the arithmetic means of the historical NM time series of loads i and j respectively.

$$\eta_{i,j} = \frac{c_{i,j}}{s_i s_j}, \text{ where } c_{i,j} = \frac{\sum_{k=1}^{N}\left(p_{i,k}^n - \tilde{p}_i^n\right)\left(p_{j,k}^n - \tilde{p}_j^n\right)}{N-1} \quad (17)$$

Assuming perfect correlation between the NM time series of these customers, i.e., $\eta_{i,j} = 1$, these two random variables can be shown to be linearly related with each other $p_i^n = a_i p_j^n, a_i \in \mathbb{R}$ as proved in Appendix A. Then using (13),

$$p_i^n = a_i p_j^n \Longrightarrow p_i^d - p_i^g = a_i p_j^d - a_i p_j^g \quad (18)$$

However, $\eta_{i,j} < 1$, primarily due to the different demand patterns of NM loads in a LS. As described in Appendix A, the solar generation profiles are more correlated in geographically small load sections due to similar cloud patterns. Thus, most of the correlation observed in NM time series would be due to the correlation in solar generation profiles. A solar generation meter can be placed at the NM load showing the highest average correlation in historical NM time series data with all other loads in the LS. The solar profile of this j^{th} NM load p_j^g can serve as the representative solar profile for all the NM loads in the LS. A scaling factor a_i is obtained for each NM load in the LS to account for different kVA ratings and seasonal factors such as soiling of PV panels. a_i is obtained using the historical NM time series of length N, by taking the partial derivative of the sum of squared errors with respect to a_i (19).

$$\frac{\partial \sum_{k=1}^{N}\left(p_{i,k}^n - a_i p_{j,k}^n\right)^2}{\partial a_i} = 0 \Rightarrow a_i = \frac{\sum_{k=1}^{N} p_{j,k}^n\, p_{i,k}^n}{\sum_{k=1}^{N}\left(p_{j,k}^n\right)^2} \quad (19)$$

Using the scaling factor a_i, the disaggregated solar generation of each NM load is $p_i^g = a_i p_j^g$ and the disaggregated actual demand is $p_i^d = p_i^n + a_i p_j^g$. The disaggregated solar generation and actual demand profiles of the previous week can be used to obtain the order and parameters of the auto regressive moving average (ARMA) model [32] for generating demand forecasts.

During an outage, the obtained ARMA model and a_i can be used to obtain the demand during all four restoration stages $\hat{P}_i(k), k \in \mathcal{K}$ for any i^{th} NM load in the LS. In the pre-outage stage S_1 as shown in Fig. 2[a], the NM time series P_i^{n,S_1} and the representative solar generation time series P_j^{g,S_1} of length K^{S_1} are available. These are used to obtain the disaggregated solar generation profile $P_i^{g,S_1} = a_i P_j^{g,S_1}$ and the actual demand profile $P_i^{d,S_1} = P_i^{n,S_1} + a_i P_j^{g,S_1}$. The ARMA model can then be used to obtain solar generation $\hat{P}_i^{g,K}$ and actual demand forecasts $\hat{P}_i^{d,K}$ for K future restoration time steps.

Using these forecasts, the forecasted demand in stage S_2 is $\hat{P}_i^{S_2}(k) = 0, k \in \{1,..,K^{S_2}\}$ where K^{S_2} is the time interval when the LS is energized by the restoration algorithm. The forecasted demand in stage S_3 is the actual demand forecast as PVs are offline $\hat{P}_i^{S_3}(k) = \hat{P}_i^{d,K}(k), k \in \{K^{S_2}+1,..,K^{S_3}\}$. The duration of stage S_3, $K^{S_3} - K^{S_2}$ is equal to the *'enter service delay'* as per IEEE 1547-2018. Finally, the forecasted demand in stage S_4 will be the net demand as PV systems are back online $\hat{P}_i^{S_4}(k) = \hat{P}_i^{d,K}(k) - \hat{P}_i^{g,K}(k), k \in \{K^{S_3}+1,..,K\}$. The forecasted demand during the K restoration steps is $\hat{P}_i(k) = \{\hat{P}_i^{S_3}(k), \hat{P}_i^{S_4}(k)\}, k \in \mathcal{K}$.

D. Generalized Time Dependent Net Metered Load Demand Model

Using the disaggregated pre-outage actual demand time series P_l^{d,S_1}, the pre-outage demand D_l^0 required for determining the CLPU curve $G_l(k), k \in \mathcal{K}$ for any l^{th} NM load can be obtained as $D_l^0 = P_l^{d,S_1}(K^{S_1})$. The generalized time dependent NM load demand model for the l^{th} NM load can now be obtained by summing the forecasted demand during the K restoration steps $\hat{P}_l(k)$ and the CLPU curve $G_l(k)$ scaled by TCL percentage g_l, $\bar{M}_l^L(k) = g_l G_l(k) + \hat{P}_l(k)$ as shown in (20),(21).

$$\bar{M}_l^L(k) = g_l \times \left[D_l^{p_1} + \frac{D_l^{p_2} - D_l^{p_1}}{t^{p_2} - t^{p_1}}(k-1)\Delta t\right]\left(1 - x\left(R_{l,k}^1\right)\right) + g_l \times h\left(R_{l,k}^1\right)x\left(R_{l,k}^1\right)\left(1 - x\left(R_{l,k}^2\right)\right) + g_l \times x\left(R_{l,k}^2\right)P_l^{d,S_1}(K^{S_1}) + \left(\hat{P}_l^{d,K}(k)\left(1 - x\left(R_{l,k}^3\right)\right) + \left(\hat{P}_l^{d,K}(k) - \hat{P}_l^{g,K}(k)\right)x\left(R_{l,k}^3\right)\right) \quad (20)$$

where $x(j)$, $R_{l,k}^1$ and $R_{l,k}^2$ are given by (18) and (19) and $R_{l,k}^3$ is given by (24).

$$R_{l,k}^3 = k\Delta t - (t^{p_3} - t^{p_1}) \quad (21)$$

It should be noted that this model is valid irrespective of whether t^{p_3} is larger or smaller than t^{p_2}. These demand curves $\bar{M}_l^L(k)$ as shown in Fig. 3[c], are obtained for all NM loads before running the microgrid restoration algorithm. Constraints to automatically select the correct demand from the curve based on when a NM load gets energized are presented in section IV.

SEQUENTIAL MICROGRID RESTORATION ALGORITHM

The algorithm presented here incorporates the proposed voltage regulating device constraints and NM load demand curves within sequential MILP based optimal microgrid restoration algorithms [33] and [21]. By adding constraints (1)-(4) and (8)-(12) to a MILP based dispatch or restoration

algorithm, the optimal taps $\hat{a}_{kj}^{\theta}$ and capacitor bank states $\hat{\delta}_{c,i}^{\theta}, i \in \mathcal{C}_c$, required to optimize the objective function are determined. Simultaneously, optimal DER dispatches are obtained which cause such voltages and power flows at the PCC of each AVR, such that its LDC estimates a load center voltage which will necessitate moving taps to $\hat{a}_{kj}^{\theta}$. Optimal DER dispatches will also create desired PCC voltages for capacitor banks to make them switch to the optimal state. While this proposed approach is sufficient for optimally controlling automatic AVRs and capacitor banks for optimal dispatch applications, additional points need to be considered while integrating it with MILP based optimal sequential microgrid restoration algorithms.

A. Estimating pre-outage states of voltage regulation devices:

The time step when a voltage regulation device will be restored is determined by the algorithm. At this first energization interval their pre-outage states need to be considered while dispatching the DERs. This is because their taps are operated using a motor and will thus stay locked in their pre-outage state during an outage. Moreover, due to the default time delays of their automatic controllers, these devices cannot be optimally controlled from the first energization interval itself. A MILP based approach is proposed here to utilize the limited line flow and voltage measurements from residential AMI meters to estimate pre-outage states of these devices.

Objective function: The objective function minimizes the differences between the limited pre-outage measurements and their corresponding variables (22). The least absolute value estimator which is accurate for state estimation has been used [31].

$$min \sum_{\theta\in\{a,b,c\}} \Big(\sum_{ij\in\mathcal{E}_M} \left|\bar{P}_{ij}^{\theta} - P_{ij}^{\theta}\right| + \sum_{ij\in\mathcal{E}_M} \left|\bar{Q}_{ij}^{\theta} - Q_{ij}^{\theta}\right| + \sum_{i\in\mathcal{B}_M} \left|\bar{V}_{i}^{\theta} - V_{i}^{\theta}\right| \Big),\ \mathcal{E}_M \subseteq \mathcal{E},\ \mathcal{B}_M \subseteq \mathcal{B} \quad (22)$$

The non-linear absolute value function needs to be linearized. The voltage term in (22) for instance is linearized by adding (23), where $v_i = \left|\bar{V}_i^{\theta} - V_i^{\theta}\right|$.

$$\bar{V}_i^{\theta} - V_i^{\theta} \le v_i, \text{ and } -\left(\bar{V}_i^{\theta} - V_i^{\theta}\right) \le v_i \quad (23)$$

Power flow constraints: The real and reactive line flows for the edges and nodal voltages for the nodes without voltage regulation devices are incorporated in the *DistFlow* model [28]. These constraints (24) also help in defining the microgrid topology.

$$\begin{aligned} \sum_{h:h\to i} P_{hi}^{\theta} &= \sum_{j:i\to j} P_{ij}^{\theta} + \bar{P}_i^{L,\theta} + \bar{P}_i^{G,\theta}, \forall i \in \mathcal{B} \\ \sum_{h:h\to i} Q_{hi}^{\theta} &= \sum_{j:i\to j} Q_{ij}^{\theta} + \bar{Q}_i^{L,\theta} + \bar{Q}_i^{G,\theta},\ \forall i \in \mathcal{B} \setminus \mathcal{C} \\ \sum_{h:h\to i} Q_{hi}^{\theta} &= \sum_{j:i\to j} Q_{ij}^{\theta} + \bar{Q}_i^{L,\theta} + \bar{Q}_i^{G,\theta} + \bar{Q}_i^{C,\theta},\ \forall i \in \mathcal{C} \setminus \mathcal{C}_c \\ V_i^{\theta} &= V_j^{\theta} + \bar{r}_{ij}^{\theta} P_{ij}^{\theta} + \bar{x}_{ij}^{\theta} Q_{ij}^{\theta},\ \forall ij \in \mathcal{E} \setminus \mathcal{E}_R \end{aligned} \quad (24)$$

Constraints on voltage regulation devices: Capacitor banks and AVRs are included using (1)-(4). However, both the capacitor bank's state $\delta_{c,i}$ and capacity $q_{c,i}^{\theta}$, in case the capacitor bank has steps, are included as variables in (4).

Upon solving the MILP formulation, the estimated pre-outage tap positions of each AVR $\bar{a}_{ij}^{\theta} = 0.9 + 0.00625 \sum_{n=0}^{5} \delta_{ij,n}^{\theta} (2)^n,\ ij \in \mathcal{E}_R$, and the estimated pre-outage states and kVAR values of each controllable capacitor bank $\bar{\delta}_{c,i}^{\theta}, \bar{q}_{c,i}^{\theta}, i \in \mathcal{C}_c$ are obtained. This step is completed prior to running the restoration algorithm and the bars on these estimates indicate that these will be used as parameters in the sequential microgrid restoration algorithm. Once the pre-outage state estimates and demand curves (20) are available for all NM loads, the restoration algorithm can be solved.

B. Objective function for restoration algorithm:

The objective function (25) aims to maximize the total energy restored over the K restoration time steps. Critical loads can be assigned a weight ($\bar{c}_i^{L,\theta}$) to ensure these are restored earlier.

$$max \left(\sum_{k=1}^{K} \sum_{i=1}^{N} \sum_{\theta\in\{a,b,c\}} \bar{c}_i^{L,\theta} \times P_{i,k}^{L,\theta} \times \Delta\bar{t} \right) \quad (25)$$

C. AVR and capacitor bank constraints:

After a voltage regulation device has been restored at $t = t_r \in \mathcal{K}$, while considering its estimated pre-outage state for dispatching DERs, it must then be optimally controlled from $t = t_r + 1$ onwards using the approach presented in subsections II.A-II.E. An approach is needed to ensure that estimated pre-outage states are used only in the first energization interval and states are controlled at their optimal positions from the second interval onwards. Finally, from the third interval onwards undesirable changes from the optimal tap positions and states of capacitor banks should be prevented. These logic propositions need to be integrated within the sequential microgrid restoration algorithm because the restoration time interval itself is a decision variable. This is achieved here by building upon the big-M method. The pre-outage state for AVRs ($\bar{a}_{ij}^{\theta}, ij \in \mathcal{E}_R$) is inlcuded using constraint (26) for all $k \in \mathcal{K}$. The term ($\sum_{p=1}^{k} \delta_{ij,p}^{E} - 1$) is zero only at the first energization interval.

$$-M\left(\sum_{p=1}^{k} \delta_{ij,p}^{E} - 1\right) \le V_{j,k}^{\theta} - \bar{a}_{ij}^{\theta} V_{i,k}^{\theta} \le M\left(\sum_{p=1}^{k} \delta_{ij,p}^{E} - 1\right) \quad (26)$$

Pre-outage states of capacitor banks ($\bar{\delta}_{c,i}^{\theta}, \bar{q}_{c,i}^{\theta}, i \in \mathcal{C}_c$) are included using (27), where $\mathcal{T}_3 = \left(\sum_{p=1}^{k} \delta_{i,p}^{N} - 1\right), \forall k \in \mathcal{K}$.

$$\sum_{h:h\to i} Q_{hi,k}^{\theta} - \left(\sum_{j:i\to j} Q_{ij,k}^{\theta} + Q_{i,k}^{L,\theta} + Q_{i,k}^{G,\theta} + \bar{\delta}_{c,i}^{\theta} \bar{q}_{c,i}^{\theta} \right) \le M\mathcal{T}_3$$

$$\sum_{h:h\to i} Q_{hi,k}^{\theta} - \left(\sum_{j:i\to j} Q_{ij,k}^{\theta} + Q_{i,k}^{L,\theta} + Q_{i,k}^{G,\theta} + \bar{\delta}_{c,i}^{\theta} \bar{q}_{c,i}^{\theta} \right) \ge -M\mathcal{T}_3 \quad (27)$$

The nodes connected to the AVRs and capacitor banks are not disconnected after being energized. This is ensured by using (28) and (29). In fact, these constraints ensure that all edges and nodes stay energized after being restored.

$$\delta_{ij,k}^{E} - \delta_{ij,k-1}^{E} \ge 0,\ k > 1,\ \forall (ij) \in \mathcal{E} \quad (28)$$

$$\delta_{i,k}^{N} - \delta_{i,k-1}^{N} \ge 0,\ k > 1,\ \forall i \in \mathcal{B} \quad (29)$$

From the second interval onwards, the optimal tap positions of AVRs ($\forall ij \in \mathcal{E}_R, k > 1$) are evaluated using (30)-(31). For 3-phase AVRs, taps on all three phases are constrained to be equal by adding $\delta_{ij,n,k}^{a} = \delta_{ij,n,k}^{b} = \delta_{ij,n,k}^{c}$. The AVR PCC voltages and line flows are controlled using constraints (32)-(34) to move taps

to their optimal positions. The term $\mathcal{T}_4 = \left(2\delta^E_{ij,k-1} - 1 - \sum_{p=1}^{k}\delta^E_{ij,p} + \sum_{p=1}^{k-1}\delta^E_{ij,p}\right)$ ensures that constraints (30)-(34) are satisfied at equality only from the second AVR energization interval onwards. Here $\mathcal{T}_1 = (V^\theta_{j,k} - P^\theta_{jh,k} r^{\theta,l}_{ij} - Q^\theta_{jh,k} x^{\theta,l}_{ij}, h{:}\, j \rightarrow h)$, $\mathcal{T}_2 = \left(\left(0.9 + 0.00625\sum_{n=0}^{5}\delta^\theta_{ij,n,k}\,(2)^n\right) - 1\right)$, $\mathcal{T}_5 = \left(1 - \delta^\theta_{ij,4,k}\right)$, $\mathcal{T}_6 = \left(1 - \delta^\theta_{ij,5,k}\right)$ and $\mathcal{T}_7 = \left(\sum_{n=4}^{5}\delta^\theta_{ij,n,k}\right)$ as described in section II.

$$-M\mathcal{T}_4 \le V^\theta_{j,k} - V^\theta_{i,k}\left(0.9 + 0.00625\sum_{n=0}^{5}\delta^\theta_{ij,n,k}\,(2)^n\right) \le M\mathcal{T}_4 \quad (30)$$

$$-M\mathcal{T}_4 \le \sum_{n=0}^{5}\delta^\theta_{ij,n,k}\,(2)^n \le 32 + M\mathcal{T}_4 \quad (31)$$

$$-M(\mathcal{T}_4 + \mathcal{T}_5) \le \mathcal{T}_1 - V^{\theta,l}_{ij} + \frac{D^{\theta,l}_{ij}}{2} + \mathcal{T}_2 \le M(\mathcal{T}_4 + \mathcal{T}_5) \quad (32)$$

$$-M(\mathcal{T}_4 + \mathcal{T}_6) \le \mathcal{T}_1 - V^{\theta,l}_{ij} + D^{\theta,l}_{ij}/2 + \mathcal{T}_2 \le M(\mathcal{T}_4 + \mathcal{T}_6) \quad (33)$$

$$-M(\mathcal{T}_4 + \mathcal{T}_7) \le \mathcal{T}_1 - V^{\theta,l}_{ij} - D^{\theta,l}_{ij}/2 + \mathcal{T}_2 \le M(\mathcal{T}_4 + \mathcal{T}_7) \quad (34)$$

Once the AVRs have been moved to their optimal tap positions, these are maintained in those positions for the remaining restoration intervals ($\forall ij \in \mathcal{E}_R, k > 2$) to prevent undesirable tap changes using constraint (35), where $\mathcal{T}_8 = \left(3\delta^E_{ij,k-2} - 1 - \sum_{p=1}^{k}\delta^E_{ij,p} + \sum_{p=1}^{k-2}\delta^E_{ij,p}\right)$.

$$-M\mathcal{T}_8 \le \delta_{ij,n,k} - \delta_{ij,n,k-1} \le M\mathcal{T}_8,\ \forall n \in \{0,..,5\} \quad (35)$$

For all capacitor banks the optimal state (ON or OFF) is determined using (36), where $\mathcal{T}_9 = \left(\sum_{p=1}^{k}\delta^N_{i,p} - 2\right)$. As described in section II, the capacitor bank is controlled to reach the optimal state using (37), (38).

$$-M\mathcal{T}_9 \le \sum_{h:h\rightarrow i} Q^\theta_{hi,k} - \Big(\sum_{j:i\rightarrow j} Q^\theta_{ij,k} + Q^{L,\theta}_{i,k} + Q^{G,\theta}_{i,k} + \delta^{c,\theta}_{i,k}\bar{Q}^{C,\theta}_i\Big) \le M\mathcal{T}_9,\ \forall i \in \mathcal{C}_c, k > 1 \quad (36)$$

$$-M\left(\mathcal{T}_9 + 1 - \delta^{c,\theta}_{i,k}\right) \le V^\theta_{i,k} - V^{\theta,on}_i \le M\left(\mathcal{T}_9 + 1 - \delta^{c,\theta}_{i,k}\right) \quad (37)$$

$$-M\left(\mathcal{T}_9 + \delta^{c,\theta}_{i,k}\right) \le V^\theta_{i,k} - V^{\theta,of}_i \le M\left(\mathcal{T}_9 + \delta^{c,\theta}_{i,k}\right) \quad (38)$$

It should be noted that unlike AVRs where constraints (30)-(34) have to be applied continuously to maintain taps in their optimal positions, for capacitor banks constraints (36)-(38) only have to be applied at their second restoration interval. Thereafter capacitor banks' nodal voltages are maintained within their dead bands using (39), where $\mathcal{T}_{10} = \left(3\delta^N_{i,k-2} - 1 - \sum_{p=1}^{k}\delta^N_{i,p} + \sum_{p=1}^{k-2}\delta^N_{i,p}\right)$. This is because capacitor banks tend to have larger deadbands and maintaining their PCC voltage continuously beyond their ON or OFF thresholds can lead to infeasibility.

$$-M\mathcal{T}_{10} + \bar{V}^{\theta,on}_i \le V^\theta_{i,k} \le \bar{V}^{\theta,of}_i + M\mathcal{T}_{10},\ \forall i \in \mathcal{C}_c, k > 2 \quad (39)$$

D. NM load constraints:

The combined NM and CLPU curves ($\bar{M}^{L,\theta}_i$) are generated for each i^{th} NM load using (23) as described in section III, before running the microgrid restoration algorithm. These curves thus act as parameters for the restoration algorithm. However, the point on the demand curve to be selected at each restoration step is determined by the restoration algorithm based on when the NM load is energized. This is achieved using (40) which has been adapted from [21] to work with non-monotonically decreasing demand curves as well. Here $\bar{P}^{L,\theta}_i, \bar{Q}^{L,\theta}_i$ are the rated real and reactive power demands of the NM load.

$$P^{L,\theta}_{i,k} = \bar{P}^{L,\theta}_i\left(\delta^N_{i,k}\bar{M}^{L,\theta}_{i,1} - \sum_{p=1}^{k}\Delta M^{L,\theta}_i(p)\delta^N_{i,k-p+1}\right)$$

$$Q^{L,\theta}_{i,k} = \bar{Q}^{L,\theta}_i\left(\delta^N_{i,k}\bar{M}^{L,\theta}_{i,1} - \sum_{p=1}^{k}\Delta M^{L,\theta}_i(p)\delta^N_{i,k-p+1}\right) \quad (40)$$

$$\text{where, } \Delta M^{L,\theta}_i(p) = \begin{cases} 0 & \text{,if } p = 1 \\ \bar{M}^{L,\theta}_{i,p-1} - \bar{M}^{L,\theta}_{i,p} & \text{,if } p > 1 \end{cases}$$

Linearized power flow constraints such as (24) are added for non-voltage regulation device nodes. Additionally, demand generation balance, maximum and minimum generation limits, voltage, and line loading limits are added as constraints. Connectivity and sequencing constraints [33] to ensure the creation of a feasible radial microgrid topology while utilizing the normally open tie-switches are also included.

CASE STUDY

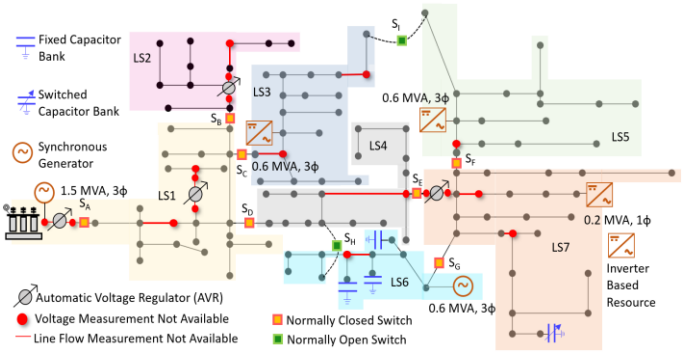

Fig. 3. Extended IEEE 123-node test feeder in OpenDSS used as a microgrid

The proposed methodology has been validated using the IEEE 123-node distribution system model as a microgrid in OpenDSS. This 3-phase unbalanced non-linear power flow model has detailed models for loads, generators, AVRs with LDCs, capacitor banks and their localized controllers, and other power delivery and conversion equipment. The $\bar{r}^\theta_{ij} + j\bar{x}^\theta_{ij}$ parameters are determined once at the peak loading condition using $\bar{r}^\theta_{ij} = real\left(\frac{V^\theta_i - V^\theta_j}{I^\theta_{ij}}\right)$ and $\bar{x}^\theta_{ij} = imag\left(\frac{V^\theta_i - V^\theta_j}{I^\theta_{ij}}\right)$. The linearized power flow algorithm requires traversing the nodes of the directed graph in order which is done using breadth first search. The feeder has a 3-phase AVR on bus 150, a 1-phase AVR on bus 9, two 1-phase AVRs on bus 25 and three 1-phase AVRs on bus 160 as shown in Fig. 3. The AVRs have unmonitored automatic LDCs with no remote-control capabilities and have unique $\bar{r}^{\theta,v}_{kj}, \bar{x}^{\theta,v}_{kj}, \bar{V}^{\theta,l}_{kj}$ and $\bar{D}^{\theta,l}_{kj}$ settings. A voltage-based controller is added to one of the four capacitor banks for testing the methodology. The presence of 2 normally open tie switches and 7 normally closed switches creates 7 load sections in the microgrid. All the 91 loads have a small rooftop PV system making them NM loads and 5 large dispatchable DERs have been added randomly in the load sections.

A. Impact of Voltage Regulation Devices' States on Voltages

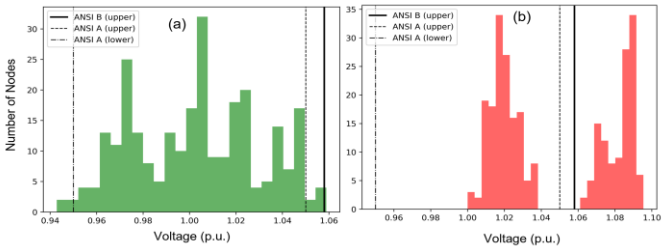

Fig. 4. Histogram of nodal voltages in IEEE 123-node system when AVR taps (a) are considered, (b) not considered, while optimally dispatching DERs

To demonstrate the importance of considering device states during microgrid restoration, an outage is created in the 123-node OpenDSS model during high loading conditions. The AVRs are locked in higher tap positions and the capacitor banks are ON. Two optimal power flow (OPF) problems are solved. In the first OPF, states are estimated using the MILP formulation proposed in section II and are used while dispatching DERs. In the second OPF, DERs are dispatched assuming all devices are in the neutral position as is typically done. Both OPFs converge, however, on applying their optimal DER dispatch in the OpenDSS model, only the first OPF is able to maintain voltages within the desired ANSI A Range as shown in Fig. 4(a). Much higher voltages are observed when device states are not considered as can be seen in Fig. 4(b). Such high voltages can trip inverters leading to microgrid restoration failure.

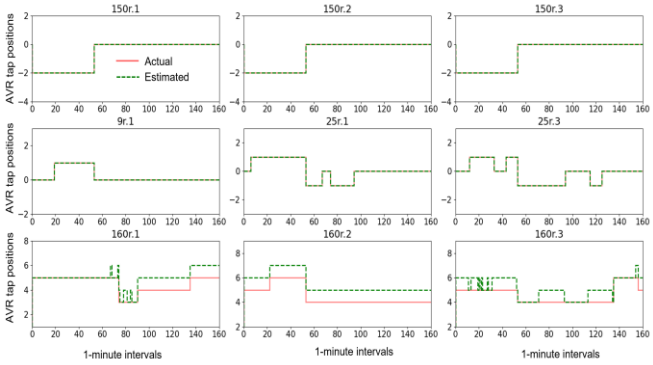

Fig. 5. Tap estimation results with limited measurements using MILP formulation proposed in section II

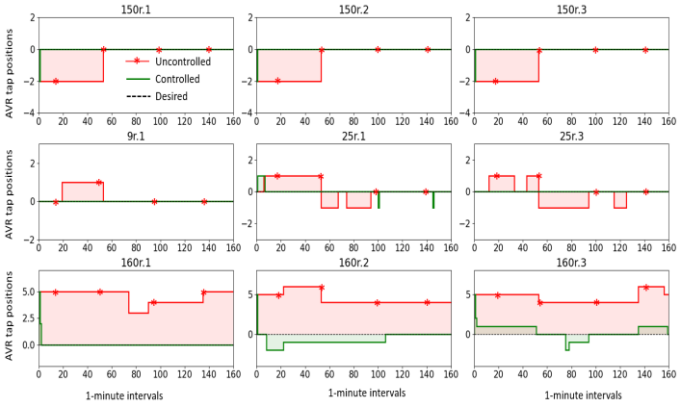

Fig. 6. Taps controlled at neutral position (tap=0) throughout the QSTS simulation using the methodology proposed in section II

B. Quasi Static Time Series Validations using OpenDSS

Quasi Static Time Series (QSTS) simulations [34] are performed at 1-minute resolution for several hours in the OpenDSS model with unique load and PV irradiance profiles. Intermittency in solar generation results in bidirectional power flows and voltage changes causing the AVRs to change tap positions. The controllable capacitor bank stays in the OFF position. These QSTS simulations are used to validate the effectiveness of the methodology proposed in section II.

In the first QSTS simulation, limited line flow and voltage measurements are used to estimate device states using the MILP formulation proposed in section II.F. The randomly chosen lines and buses shown in red in Fig. 3 do not have AMI meters. Fig. 5 shows a comparison of the actual tap positions observed in OpenDSS and the estimated tap positions. The proposed MILP formulation can accurately estimate tap positions throughout the QSTS simulation, with a maximum deviation of only 1 tap position out of the 33 possible tap positions.

The QSTS simulations are performed again, and in this second run, DERs are dispatched optimally while controlling the AVRs to be at the neutral position (tap=0) using the optimal control approach proposed in section II. Fig. 6 shows a comparison of the uncontrolled tap positions, the controlled tap positions, and the desired tap position. The proposed methodology is able to control the tap positions of all the unmonitored AVRs with automatic LDC's at the desired neutral tap position. Minor deviations observed are due to the use of linearized power flow versus the non-linear power flow used in OpenDSS. The controllable capacitor bank also stays in the OFF position throughout the QSTS simulation. Solving each OPF to estimate device states takes 0.7 seconds on average and it takes 0.33 seconds to solve each OPF for controlling device states. OPF is formulated in the Python package PYOMO and the GLPK solver is used.

C. Sequential Microgrid Restoration Results

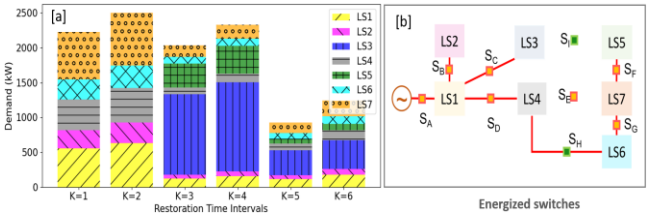

Fig. 7. [a] Restoration sequence of load sections and their demand during each microgrid restoration interval; [b] Switches energized to restore all load sections of the microgrid

Sequential microgrid restoration is completed in $K = 6$ time intervals using the proposed methodology. AVRs are locked at their respective pre-outage tap positions of time interval 1 as shown in Fig. 5. All loads are NM loads with a 40% TCL percentage [22]. Pecan street database [35] is used to obtain solar generation and demand profiles for the NM loads. Using the methodology proposed in section III, demand forecasts $\bar{M}_i^L(k)$ which include the CLPU demand, are obtained for each NM load for the 6 restoration intervals.

The switches energized to restore all 7 load sections and the sequence in which they are energized can be seen in Fig. 7. This figure shows that the demand of each load section follows the expected pattern shown in Fig. 2[c]. For instance, LS3 is

energized at interval 3 and shows high demand due to the combined effect of PVs being offline and CLPU. The demand then increases to peak demand in interval 4 as TCL diversity is lost. Then from interval 5 onwards the PV systems are back online after their *'enter service delay'* and demand reduces. Fig. 7[b] shows that normally open tie switches are used to meet all the constraints while maintaining a radial topology.

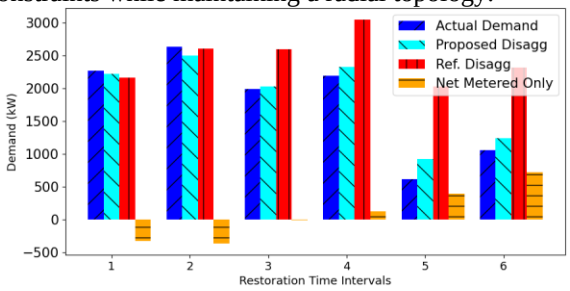

Fig. 8. Comparison of actual demand with demand forecasts obtained using the approach proposed in section III, disaggregation approach in [25], and only net metered time series data.

Figure 8 presents a comparison of the forecasted versus actual demands observed during the 6 restoration intervals. The *actual demand* is obtained by summing the demand, solar generation and the CLPU demand. The forecasted demand using the proposed disaggregation methodology (*Proposed Disagg*) in section III required only one solar generation meter per load section. This meter is deployed at the NM load exhibiting the highest average correlation in historical NM time series data with all other NM loads in the load section. The *Proposed Disagg* demand is compared with the disaggregation approach (*Ref. Disagg*) proposed in [25]. 3 randomly deployed solar generation meters per load section are used for the *Ref. Disagg* approach. The demand forecasts using only the historical NM time series (*Net Metered Only*), while ignoring the *'enter service delay'* and CLPU phenomenon are also presented. The *Proposed Disagg* approach generates the most accurate NM demand forecasts in all 6 restoration time intervals. The accuracy of forecasts obtained using the *Ref. Disagg* approach decreases significantly as time horizon increases. Using only the NM time series-based forecasts causes large demand generation imbalance, leading to frequency instability and restoration failure.

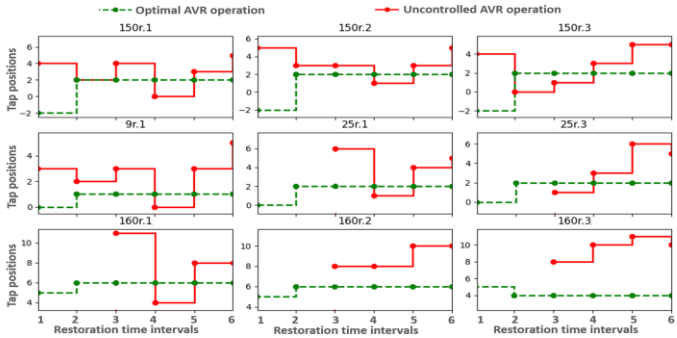

Fig. 9. AVR tap positions during microgrid restoration with and without the proposed optimal control approach.

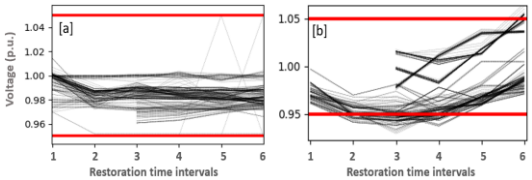

Fig. 10. All nodal voltages during microgrid restoration [a] with, and [b] without the proposed optimal control approach

Figures 9 and 10 show the AVR tap positions and all nodal voltages during the 6 restoration intervals, with and without the application of the optimal control approach proposed in this paper. These figures show that when AVR operation is not coordinated with DER dispatch, frequent large tap changes are seen leading to both over and under voltages and possibly restoration failure. Using the proposed optimal control approach, AVRs are energized while considering their estimated pre-outage states. At their second energization interval, the optimal tap position is evaluated and such AVR PCC voltage and line flows are created which makes their automatic LDC to command the taps to move to their optimal tap position. From the third energization interval onwards, the taps are maintained at these optimal tap positions, while maintaining all nodal voltages within the ANSI limits throughout the successful sequential microgrid restoration.

CONCLUSIONS

An approach to reduced time and cost of deployment of microgrids is to not depend on communications and remote-control capabilities. The integrated approach proposed in this paper mitigates the need for adding such capabilities in unmonitored automatic voltage regulation devices and net metered loads by incorporating their time dependent behavior in a sequential optimal microgrid restoration algorithm. This approach allows coordinated optimal control of dispatchable distributed energy resources with non-remote control capable voltage regulation devices. Through a case study on the unbalanced IEEE 123-node test system, the effectiveness of the proposed approach in optimally controlling voltage regulation devices' states has been demonstrated. The proposed disaggregation based net metered load demand model is also shown to accurately forecast net metered load demand during all time steps of the microgrid restoration process. To reduce computation time, voltage drops across voltage regulators are ignored and simplified power flow expressions are used. This however can reduce accuracy which can be further improved by using power flow expressions that consider coupling among phases. Future work would also include integration of optimization and control algorithms for managing dynamics that arise due to sudden load energization during restoration.

APPENDIX A

UNITY CORRELATION COEFFICIENT AND LINEARITY

Proof: Assuming that any two net metered random variables p_i^n, p_j^n are linearly related $p_i^n = a_i p_j^n,\ a_i \in \mathbb{R}^1$, the covariance $c_{i,j}$ between them is defined as the expected value of the outer product of $(p_i^n - \mathbb{E}[p_i^n])$ and $\left(p_j^n - \mathbb{E}[p_j^n]\right)$. Given the net

metered time series of these two variables, their expected values will be their arithmetic means, $\mathbb{E}[p_i^n] = \tilde{p}_i^n$ and $\mathbb{E}[p_j^n] = \tilde{p}_j^n$. Hence,

$$c_{i,j} = \mathbb{E}\left[(p_i^n - \tilde{p}_i^n)(p_j^n - \tilde{p}_j^n)\right] \quad (41)$$

$$= \mathbb{E}[p_i^n p_j^n] - \tilde{p}_j^n \mathbb{E}[p_i^n] - \tilde{p}_i^n \mathbb{E}[p_j^n] + \tilde{p}_i^n \tilde{p}_j^n \quad (42)$$

$$= \mathbb{E}[p_i^n p_j^n] - \tilde{p}_i^n \tilde{p}_j^n = \mathbb{E}[p_i^n p_j^n] - \mathbb{E}[p_i^n]\mathbb{E}[p_j^n] \quad (43)$$

Squaring the correlation coefficient defined in (20),

$$(\eta_{i,j})^2 = \frac{(c_{i,j})^2}{(s_i)^2 (s_j)^2} = \frac{\left(\mathbb{E}[p_i^n p_j^n] - \mathbb{E}[p_i^n]\mathbb{E}[p_j^n]\right)^2}{(s_i)^2 (s_j)^2} \quad (44)$$

Substituting, $p_i^n = a_i p_j^n$ in the numerator,

$$(\eta_{i,j})^2 = \frac{\left(a_i \mathbb{E}\left[(p_j^n)^2\right] - a_i (\mathbb{E}[p_j^n])^2\right)^2}{(s_i)^2 (s_j)^2} \quad (45)$$

The variance $(s_j)^2$ is defined as,

$$(s_j)^2 = \mathbb{E}[p_j^n - \tilde{p}_j^n]^2 = \mathbb{E}\left[(p_j^n)^2\right] - 2\tilde{p}_j^n \mathbb{E}[(p_j^n)] + \mathbb{E}\left[(\tilde{p}_j^n)^2\right] \quad (46)$$

$$= \mathbb{E}\left[(p_j^n)^2\right] - 2(\tilde{p}_j^n)^2 + (\tilde{p}_j^n)^2 = \mathbb{E}\left[(p_j^n)^2\right] - (\tilde{p}_j^n)^2 \quad (47)$$

$$= \mathbb{E}\left[(p_j^n)^2\right] - (\mathbb{E}[p_j^n])^2 \quad (48)$$

Substituting (48) in the numerator of (45),

$$(\eta_{i,j})^2 = \frac{a_i^2 \left((s_j)^2\right)^2}{(s_i)^2 (s_j)^2} \quad (49)$$

Also, the variance $(s_i)^2 = a_i^2 (s_j)^2$ since $p_i^n = a_i p_j^n$, hence,

$$(\eta_{i,j})^2 = \frac{a_i^2 \left((s_j)^2\right)^2}{a_i^2 (s_j)^2 (s_j)^2} = 1 \quad (50)$$

Thus, if $\eta_{i,j} = 1$, one can express $p_i^n = a_i p_j^n$, $a_i \in \mathbb{R}^1$. In practice however, $\eta_{i,j}$ will be less than 1 primarily due to the low correlation in the actual demand time series of NM loads. The solar generation profiles of NM loads in a geographically small load section with similar cloud patterns will be more correlated. This was validated by evaluating the correlation in actual demand time series of 18 residential customers from the Pecan Street database which is found to be 0.306 whereas the correlation in their solar generation time series is 0.921 [32]. This is why solar generation is expressed as a linear function of the representative profile in section III.

REFERENCES

[1] C. -C. Liu *et al*., "Microgrid Building Blocks: Concept and Feasibility," *IEEE Open Access Journal of Power and Energy*, vol. 10, pp. 463-476, 2023.

[2] S. Cai, Y. Xie, Q. Wu, M. Zhang, X. Jin, and Z. Xiang, "Distributionally Robust Microgrid Formation Approach for Service Restoration Under Random Contingency," *IEEE Transactions on Smart Grid*, vol. 12, no. 6, pp. 4926–4937, 2021.

[3] X. Yang *et al*., "Cooperative Repair Scheduling and Service Restoration for Distribution Systems with Soft Open Points," *IEEE Transactions on Smart Grid*, vol. 14, no. 3, pp. 1827–1842, 2023.

[4] S. Poudel and A. Dubey, "Critical Load Restoration Using Distributed Energy Resources for Resilient Power Distribution System," *IEEE Transactions on Power Systems*, vol. 34, no. 1, pp. 52–63, 2019.

[5] A. S. Alahmed and L. Tong, "On Net Energy Metering X: Optimal Prosumer Decisions, Social Welfare, and Cross-Subsidies," *IEEE Transactions on Smart Grid*, vol. 14, no. 2, pp. 1652–1663, 2023

[6] M. Farrokhabadi *et al.*, "Microgrid Stability Definitions, Analysis, and Examples," *IEEE Transactions on Power Systems*, vol. 35, no. 1, pp. 13–29, 2020.

[7] M. J. Reno, S. Brahma, A. Bidram, and M. E. Ropp, "Influence of Inverter-Based Resources on Microgrid Protection: Part 1: Microgrids in Radial Distribution Systems," *IEEE Power and Energy Magazine*, vol. 19, no. 3, pp. 36–46, 2021.

[8] M. Lave, M. J. Reno, and R. J. Broderick, "Characterizing Local High-Frequency Solar Variability and its Impact to Distribution Studies," *Solar Energy*, vol. 118, pp. 327–337, 2015.

[9] M. J. Reno, M. Lave, J. E. Quiroz, and R. J. Broderick, "PV Ramp Rate Smoothing Using Energy Storage to Mitigate Increased Voltage Regulator Tapping," in *2016 IEEE 43rd Photovoltaic Specialists Conference (PVSC)*, 2016, pp. 2015–2020.

[10] H. M. M. Maruf and B. H. Chowdhury, "Impact of Smart Inverter Functions on Dynamic Step Voltage Regulator Settings for Distribution Voltage Control," in *2019 IEEE Milan PowerTech*, 2019, pp. 1–6.

[11] H. Sekhavatmanesh and R. Cherkaoui, "Analytical Approach for Active Distribution Network Restoration Including Optimal Voltage Regulation," *IEEE Transactions on Power Systems*, vol. 34, no. 3, pp. 1716–1728, 2019.

[12] R. Sadnan, S. Poudel, A. Dubey, and K. P. Schneider, "Layered Coordination Architecture for Resilient Restoration of Power Distribution Systems," *IEEE Transactions on Industrial Informatics*, pp. 1–1, 2022.

[13] W. H. Kersting, *Distribution System Modeling and Analysis*. Fourth Edition, CRC Press, 2017.

[14] A. Bedawy, N. Yorino, K. Mahmoud, Y. Zoka, and Y. Sasaki, "Optimal Voltage Control Strategy for Voltage Regulators in Active Unbalanced Distribution Systems Using Multi-Agents," *IEEE Transactions on Power Systems*, vol. 35, no. 2, pp. 1023–1035, 2020.

[15] K. Horowitz, "2019 Distribution System Upgrade Unit Cost Database Current Version," Jan. 2019.

[16] "California distributed generation statistics." https://www.californiadgstats.ca.gov/charts/

[17] Y. Yao, F. Ding, K. Horowitz, and A. Jain, "Coordinated Inverter Control to Increase Dynamic PV Hosting Capacity: A Real-Time Optimal Power Flow Approach," *IEEE Systems Journal*, vol. 16, no. 2, pp. 1933–1944, 2022.

[18] F. Kabir, N. Yu, W. Yao, R. Yang, and Y. Zhang, "Joint Estimation of Behind-the-Meter Solar Generation in a Community," *IEEE Transactions on Sustainable Energy*, vol. 12, no. 1, pp. 682–694, 2021.

[19] "IEEE Standard for Interconnection and Interoperability of Distributed Energy Resources with Associated Electric Power Systems Interfaces," *IEEE Std 1547-2018 (Revision of IEEE Std 1547-2003)*, pp. 1–138, 2018.

[20] K. P. Schneider, E. Sortomme, S. S. Venkata, M. T. Miller, and L. Ponder, "Evaluating the Magnitude and Duration of Cold Load Pick-up on Residential Distribution using Multi-State Load Models," *IEEE Transactions on Power Systems*, vol. 31, no. 5, pp. 3765–3774, 2016.

[21] B. Chen, C. Chen, J. Wang, and K. L. Butler-Purry, "Multi-Time Step Service Restoration for Advanced Distribution Systems and Microgrids," *IEEE Transactions on Smart Grid*, vol. 9, no. 6, pp. 6793–6805, 2018.

[22] M. Song, R. R. Nejad, and W. Sun, "Robust Distribution System Load Restoration with Time-Dependent Cold Load Pickup," *IEEE Transactions on Power Systems*, vol. 36, no. 4, pp. 3204–3215, 2021.

[23] K. Li, Y. Wang, N. Zhang, and F. Wang, "Precision and Accuracy Co-Optimization-Based Demand Response Baseline Load Estimation Using Bidirectional Data," *IEEE Transactions on Smart Grid*, vol. 14, no. 1, pp. 266–276, 2023.

[24] K. Li, F. Wang, Z. Mi, M. Fotuhi-Firuzabad, N. Duić, and T. Wang, "Capacity and Output Power Estimation Approach of Individual Behind-the-Meter Distributed Photovoltaic System for Demand Response Baseline Estimation," *Applied Energy*, vol. 253, p. 113595, 2019.

[25] K. Li, J. Yan, L. Hu, F. Wang, and N. Zhang, "Two-Stage Decoupled Estimation Approach of Aggregated Baseline Load Under High Penetration of Behind-the-Meter PV System," *IEEE Transactions on Smart Grid*, vol. 12, no. 6, pp. 4876–4885, 2021.

[26] T. Ding, Z. Wang, M. Qu, Z. Wang, and M. Shahidehpour, "A Sequential Black-Start Restoration Model for Resilient Active Distribution Networks," *IEEE Transactions on Power Systems*, vol. 37, no. 4, pp. 3133–3136, 2022.

[27] "OpenDSSDirect.py." https://github.com/dss-extensions/OpenDSSDirect.py

[28] M. E. Baran and F. F. Wu, "Network Reconfiguration in Distribution Systems for Loss Reduction and Load Balancing," *IEEE Transactions on Power Delivery*, vol. 4, no. 2, pp. 1401–1407, 1989.

[29] W. Wu, Z. Tian, and B. Zhang, "An Exact Linearization Method for OLTC of Transformer in Branch Flow Model," *IEEE Transactions on Power Systems*, vol. 32, no. 3, pp. 2475–2476, 2016.

[30] H. Nagarajan, M. Lu, E. Yamangil, and R. Bent, "Tightening McCormick Relaxations for Nonlinear Programs via Dynamic Multivariate

Partitioning," in *Principles and practice of constraint programming*, Springer International Publishing, 2016.
[31] A. Gandluru, S. Poudel, and A. Dubey, "Joint Estimation of Operational Topology and Outages for Unbalanced Power Distribution Systems," *IEEE Transactions on Power Systems*, vol. 35, no. 1, pp. 605–617, 2020.
[32] A. K. Jain, C.-C. Liu, K. P. Schneider, F. K. Tuffner, and D. Ton, "Demand Estimation of Net Metered Loads for Microgrid Restoration," in *2023 IEEE Power & Energy Society Innovative Smart Grid Technologies Conference (ISGT)*, 2023, pp. 1–5.
[33] B. Chen, C. Chen, J. Wang, and K. L. Butler-Purry, "Sequential Service Restoration for Unbalanced Distribution Systems and Microgrids," *IEEE Transactions on Power Systems*, vol. 33, no. 2, pp. 1507–1520, 2018.
[34] A. K. Jain, N. Sahani, and C.-C. Liu, "Detection of Falsified Commands on a DER Management System," *IEEE Transactions on Smart Grid*, vol. 13, no. 2, pp. 1322–1334, 2022.
[35] "Pecan street dataport." https://www.pecanstreet.org/dataport/.